

Phase-Change-Enabled, Rapid, High-Resolution Direct Ink Writing of Soft Silicone

Yiliang Wang* and Norbert Willenbacher*

Soft silicone is an ideal flexible material for application, e.g., in soft robotics, flexible electronics, bionics, or implantable biomedical devices. However, gravity-driven sagging, filament stretching, and deformation can cause inevitable defects during rapid manufacturing, making it hard to obtain complex, high-resolution 3D silicone structures with direct ink writing (DIW) technology. Here, rapid DIW of soft silicone enabled by a phase-change-induced, reversible change of the ink's hierarchical microstructure is presented.

During printing, the silicone-based ink, containing silica nanoparticles and wax microparticles, is extruded from a heated nozzle into a cold environment under controlled stress. The wax phase change (solid–liquid–solid) during printing rapidly destroys and rebuilds the particle networks, realizing fast control of the ink flow behavior and printability. This high-operating-temperature DIW method is fast (maximum speed $\approx 3100 \text{ mm min}^{-1}$) and extends the DIW scale range of soft silicone. The extruded filaments have small diameters ($50 \pm 5 \text{ }\mu\text{m}$), and allow for large spans (≈ 13 -fold filament diameter) and high aspect ratios (≈ 1), setting a new benchmark in the DIW of soft silicone. Printed silicone structures exhibit excellent performance as flexible sensors, superhydrophobic surfaces, and shape-memory bionic devices, illustrating the potential of the new 3D printing strategy.

1. Introduction

Soft silicone, due to its excellent flexibility, resilience, stability, and biocompatibility, plays a prominent role in soft robotics,^[1–4] flexible electronics,^[5,6] biomedical devices,^[7,8] and bionics.^[9–11] However, its intrinsic viscoelastic softness makes it hard to fabricate complex 3D structures with traditional methods.

Y. Wang, N. Willenbacher
Institute of Mechanical Process Engineering and Mechanics
Karlsruhe Institute of Technology
Karlsruhe 76131, Germany
E-mail: wangyiliang1988@163.com; norbert.willenbacher@kit.edu

Y. Wang
Department of Chemistry
Tsinghua University
Beijing 100084, China

 The ORCID identification number(s) for the author(s) of this article can be found under <https://doi.org/10.1002/adma.202109240>.

© 2022 The Authors. Advanced Materials published by Wiley-VCH GmbH. This is an open access article under the terms of the Creative Commons Attribution-NonCommercial License, which permits use, distribution and reproduction in any medium, provided the original work is properly cited and is not used for commercial purposes.

DOI: 10.1002/adma.202109240

Additive manufacturing or 3D printing has become a versatile technology for rapidly turning computer-aided designs into complex 3D objects using diverse polymers,^[12–14] but the 3D printing of high-resolution soft silicone is still a challenge. Nowadays, the 3D printing of soft silicone (i.e., poly(dimethylsiloxane), PDMS) comprises two categories: light-based 3D printing and extrusion-based 3D printing.^[13,15,16] Although the former could provide a higher printing resolution, it is limited by the expensive, biohazardous, photocurable silicone and the complicated printing process. Furthermore, its multimaterial fabrication is not universal, and most silicone composites are not suitable for light-based printing.^[16] Ink-based 3D printing methods, by contrast, own a simpler printing procedure and can pattern diverse printable inks formed by different kinds of liquid matrix and soluble materials.

Fused deposition modeling is the high operating temperature (HOT) 3D printing technology for thermoplastic polymers, where the polymeric filaments are melted and extruded through a heated nozzle, and then solidify as they cool to low temperature. Although printing at high speed (up to 500 mm s^{-1}) is possible, the high viscosity of the polymer melt limits the nozzle diameter, and the die swelling of the melt further reduces the resolution of printed structures.^[17] Direct ink writing (DIW) is another important extrusion-based 3D printing method, in which the viscoelastic ink is extruded through a nozzle and selectively deposited layer by layer. The stable shear stress in the nozzle applied by mechanical pressure must exceed the ink's yield stress for achieving the smooth flow of ink. Once extruded, such viscoelastic fluids should rapidly recover or significantly increase their viscosity and moduli, so the ink takes a gel state to retain the printed architectures, allowing for high-resolution 3D printing. Generally, this may be achieved by sudden stress reduction, phase change, solvent evaporation, gelation, and polymerization of the ink. Unfortunately, for commercial silicone formulations, the most suitable way is polymerization, which suffers from slow kinetics and a corresponding slow increase in viscosity, leading to material flow, poor resolution, and long build time.^[18] Although, many new printing strategies for soft silicone have been invented, including capillary-suspension-type^[15,19] and emulsion-type inks,^[20] as well as tailored printing concepts such as embedded

printing,^[21,22] multi-nozzle 3D printing,^[13] or other customized printing methods.^[11,18] Nevertheless, the rapid 3D printing of silicone elastomers with high resolution is still difficult to achieve, limiting their applications, especially in flexible electronics^[6,23] and smart soft devices.^[24,25] Realizing the stable extrusion of the ink and the fast control of rheological properties is the key to ink-based 3D printing of soft materials.

2. Results and Discussion

Here, we report the additive manufacturing of high-resolution soft silicone by using the PDMS/silica nanoparticle/wax microparticle (PSW) phase change ink and the HOT-DIW^[26] 3D printing system (Figure 1a,b and Figure S1a,b (Supporting Information)). The HOT-DIW system has three controllable parameters, including piston pressure (P), printhead speed (V_p), and nozzle temperature (T), which can control the printing process more precisely than the common DIW printer. The PSW ink (Figure 1c) can change and recover its rheological properties rapidly in the printing and the subsequent cooling process. The wax microparticles (average size, $3.0 \pm 0.8 \mu\text{m}$, Figure S2a,b, Supporting Information) and silica nanoparticles (fumed silica, $\approx 70 \text{ nm}$) in the ink serve as

effective rheological modifiers through creating micro- and nanoscale networks (Figure 1b).^[2,13,18] PDMS (Sylgard 184) is a liquid polymer with very low moduli and viscosity (3.5 Pa s) before curing, which does not have a yield stress. A large amount of solid particles or fillers is necessary for preparing printable PDMS inks with distinct yield stress and pronounced shear-thinning behavior, necessary to enable extrusion and then maintain the printed structures. However, such a large amount of particles results in strong aggregation, making it extremely difficult to pass through thin nozzles ($<150 \mu\text{m}$). For example, the PDMS/silica nanoparticle (PS) ink has a very low extrusion rate ($<4 \text{ mm min}^{-1}$) at which stable and effect free filaments can be obtained when a $100 \mu\text{m}$ nozzle is used (Figure S1c, Supporting Information) at $45 \text{ }^\circ\text{C}$ with a pressure of 80 bar (the maximum pressure of our printer), and it cannot be extruded out of thinner nozzles (e.g., 50 and $80 \mu\text{m}$). In PSW ink, we use a combination of wax microparticles (17.6 vol%) and silica nanoparticles (5.53 vol%) to increase the moduli and yield stress at room temperature (RT, $20 \text{ }^\circ\text{C}$), while enabling a good flow behavior at higher temperatures, due to the suitable phase change behavior of the wax (Figure S2c, Supporting Information). The PSW ink is highly elastic ($G' > G''$), its yield stress^[27] ($\tau_y = 5745 \pm 281 \text{ Pa}$) is substantially higher than that of the corresponding PS ink without wax particles ($\tau_y = 4077 \pm 211 \text{ Pa}$). The

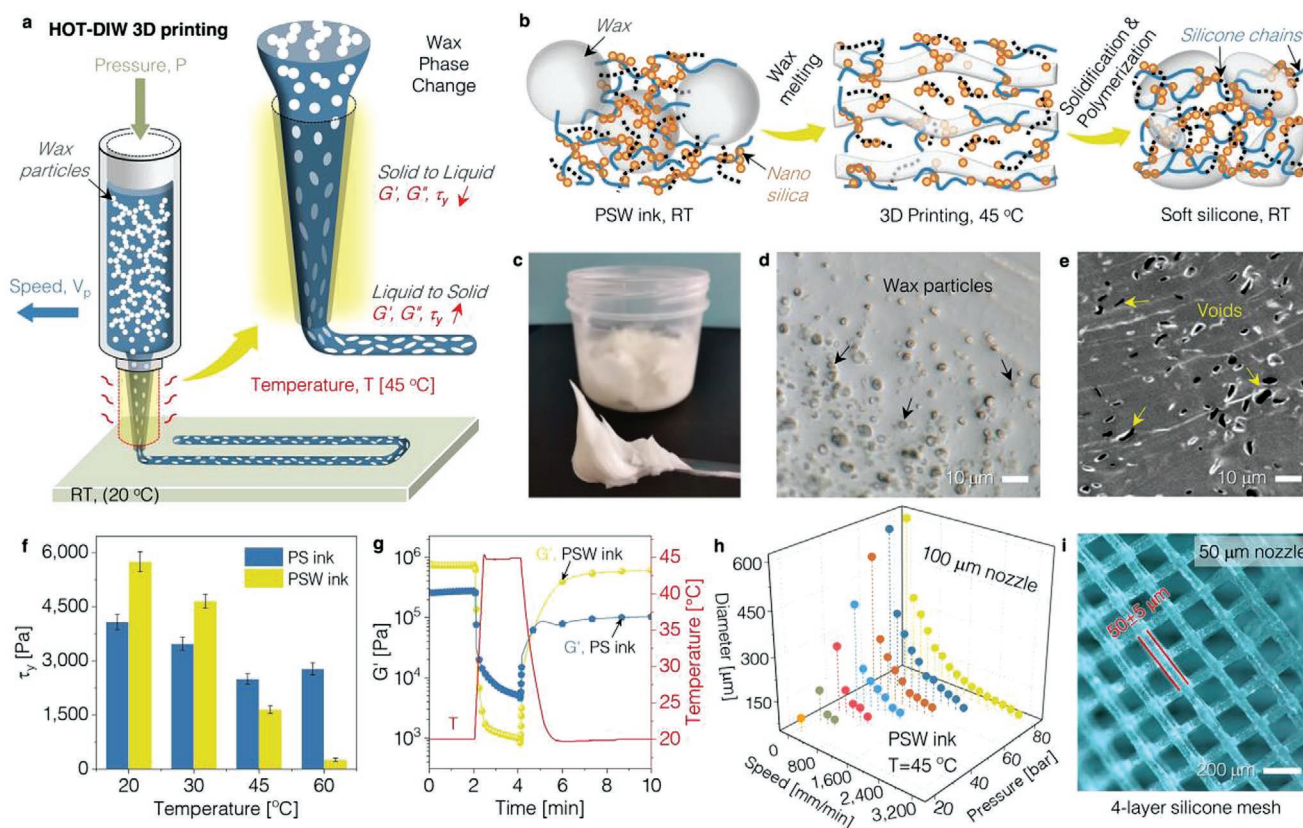


Figure 1. Phase-change-induced high-resolution 3D printing of soft silicone. a) Schematic illustration of the high-operating-temperature-direct ink writing (HOT-DIW) process. b) Scheme for the collapse and rebuild of particle networks in the PSW ink during the printing and following polymerization. c) The photograph of PSW ink. d) Wax particles in PSW ink, which is coated on glass with a squeegee. The top region corresponds to an area where the film is too thin to include particles. e) The voids in the cross-section of one printed object after removing the wax. f) Yield stress (τ_y) of PS ink and PSW ink at different temperatures. g) Response of storage modulus (G') for PS ink and PSW ink to the temperature change ($20\text{--}45\text{--}20 \text{ }^\circ\text{C}$). h) Influence of printing speed (V_p) and pressure (P) on the diameter of extruded filament. i) The $50 \mu\text{m}$ filaments in a printed silicone object.

collapse of the wax network at high temperatures above the initial solid–liquid phase change temperature (38.8 °C), however, enables the good fluidity of the PSW ink (Figure 1f,g). For instance, the yield stress values at 45 and 60 °C are $\tau_y = 1650 \pm 109$ and 260 ± 42 Pa, respectively, and the shear moduli drop by more than an order of magnitude upon melting of the wax particles (Figure 1g and Figure S2d (Supporting Information)). After passing the hot nozzle, the extruded filament cools down and the networks rebuild rapidly and the storage modulus (G') recovers to the initial value prior to melting (Figure 1g and Figure S2e (Supporting Information)) due to the fast liquid–solid phase change of the wax, and it can retain well at RT until the polymerization of the silicone happens (≈ 7 days at RT). The decrease and recovery of the shear modulus during a heating/cooling cycle is more pronounced for the PSW ink compared to PS ink (Figure 1g), which indicates the versatile temperature-sensitive flow behavior of PSW ink.

Besides, the wax particles in PSW ink (Figure 1d) are deformed into flat shapes, as proved by the long and narrow voids in the cross-section of the printed object shown in Figure 1e. To achieve good fluidity as well as fast recovery of τ_y and shear moduli, 45 °C is chosen as the printing temperature of PSW ink. At this temperature, the PSW ink can be extruded easily, which enables printing with high speed and excellent precision. For instance, the maximum speed $V_{p,max}$ and the thinnest filament diameter D for printing with 100 μm nozzle at 45 °C are $V_{p,max} = 3100 \text{ mm min}^{-1}$ and $D = 65 \pm 2 \mu\text{m}$ with a pressure of 80 bar (Figure 1h). Decreasing nozzle temperature (35 or 40 °C) shrinks the parameter (P and V_p) range for printing, higher extrusion pressure is required, and the maximum printing speed decreases (Figure S2f,g, Supporting Information). On the other hand, printing at higher temperatures (e.g., 60 °C) is not feasible since the structural recovery after nozzle passage is too slow and hence severe deformations happen. Most strikingly, the PSW ink can be printed into high-resolution soft silicone with $D = 50 \pm 5 \mu\text{m}$ using a 50 μm nozzle (Figure 1i) at 45 °C. The rapid printing process is demonstrated in Video S1 (Supporting Information).

Various soft 3D objects with high resolution and shape fidelity have been printed using the HOT-DIW printing strategy (Figure 2 and Figure S3 (Supporting Information)). In Figure 2a, the 4-layer mesh with a filament diameter D of $50 \pm 5 \mu\text{m}$ and an aspect ratio (height/diameter) of about 1 (Figure 2b,c) sets a new benchmark for DIW-type printing of soft silicone. The grid structure is regular (Figure 2b,c), and owns a very low dimensional change compared with the initial design (Figure S4a, Supporting Information). The scanning electron microscopy (SEM) image (Figure 2d) shows that there are many wax particles on the filament surface, which help to retain the printed structures. The filaments in different layers can withstand the gravity-induced deformation very well. It benefits from the high τ_y and stable solid state of PSW ink at RT, which can be proved further by the high span distance of the extruded filaments, i.e., the span S , i.e., the gap that can be bridged by a filament without significant deformation or breakage, of 100 and 50 μm filaments is about 1300 and 700 μm (Figure 2e,f), respectively, i.e., $S/D \approx 13$. This is somewhat lower than the value $S/D = 24$ theoretically predicted according to^[28]

$$G' \geq 1.4 \rho g (S/D)^4 D \quad (1)$$

where G' is the storage modulus of PSW ink (3×10^5 Pa, RT), ρ is the density (1.1 g cm^{-3}), g is the constant of gravity, and D is the filament diameter. We attribute this deviation to the limited heat transport and finite structural recovery time after nozzle passage, resulting in an initially lower storage modulus than given in Figure 1g. As for dense and thick structures, this technology also shows good performance, for instance, the printed silicone logo has a small size (8 layers, 10 mm \times 6 mm) and good resolution (Figure 2g and Figure S4b,e, Supporting Information). During the DIW printing process, gravity-driven sagging, filament stretching, and deformation at high printhead speed or when the printhead rapidly changes direction may induce defects in the printed soft objects, especially for those structures with sharp corners and thin walls (Figure S3a,b, Supporting Information). Our method has outstanding performance in printing the hollow and high, thin-walled structures. As shown in Figure 2h, the printed tiny hollow star has the same structure as the G-code document (Figure S4c, Supporting Information), and its wall thickness and layer thickness are about 300 and $47 \pm 3 \mu\text{m}$, respectively. The surfaces and cross-section of the star have supplied more details (Figure 2h and Figure S4d (Supporting Information)).

Beyond that, the printed objects can be functionalized easily without decreasing the resolution. For example, the mesh can be converted into a hierarchically structured and conductive mesh after being coated with carbon nanotubes (CNT) and another kind of silicone (Ecoflex-30) (Figure S5, Supporting Information). The functionalization process includes the high shear stirring with CNT, the swelling–shrinking treatment with mineral spirits and ethanol (Video S2, Supporting Information), and the coating with Ecoflex. During the solvent treatment, the filaments shrink and a lot of voids are generated caused by the removal of the wax (Figure 2i). The CNT is bundled on the filaments by the Ecoflex and forms an $\approx 3 \mu\text{m}$ conductive layer (Figure 2j). Many CNT aggregations and cracks can be found in the layer (Figure 2k), creating more microstructures that are sensitive to the deformation of silicone mesh. Besides, the coating process has changed the mesh color and size (Figure 2l).

Flexible and stretchable silicone with rich microstructures has many applications in flexible electronics, especially when combined with conductive nanomaterials.^[29–32] In all reported works, the geometry of the active layer has significant effects on the flexible sensor's performance.^[23,30,33] In our case, the printed meshes coated with a CNT/Ecoflex layer can be used as the sensing part of an ultrathin, flexible pressure sensor (thickness is about 300 μm ; Figure S6a–c, Supporting Information) comprised of three layers, where the sensing layer is sandwiched by two pieces of Ag/polyimide (PI) films (Figure 3a,b). Compared with the sensing layer prepared by micropatterning methods (typically prepared by molding or standard lithographic methods),^[6,23,34] the conductive meshes could control more geometries, including the layer number L , filament diameter D , and distance d (Figure 3c). These can endow sensors with a low detection limit (30 Pa), high sensitivity (57.5 kPa^{-1}), and a wide working range (0–500 kPa). The high performance arises from three response stages to the pressure, including the contact between conductive mesh and electrodes (Section I), the mesh deformation (Section II), and the contact between two

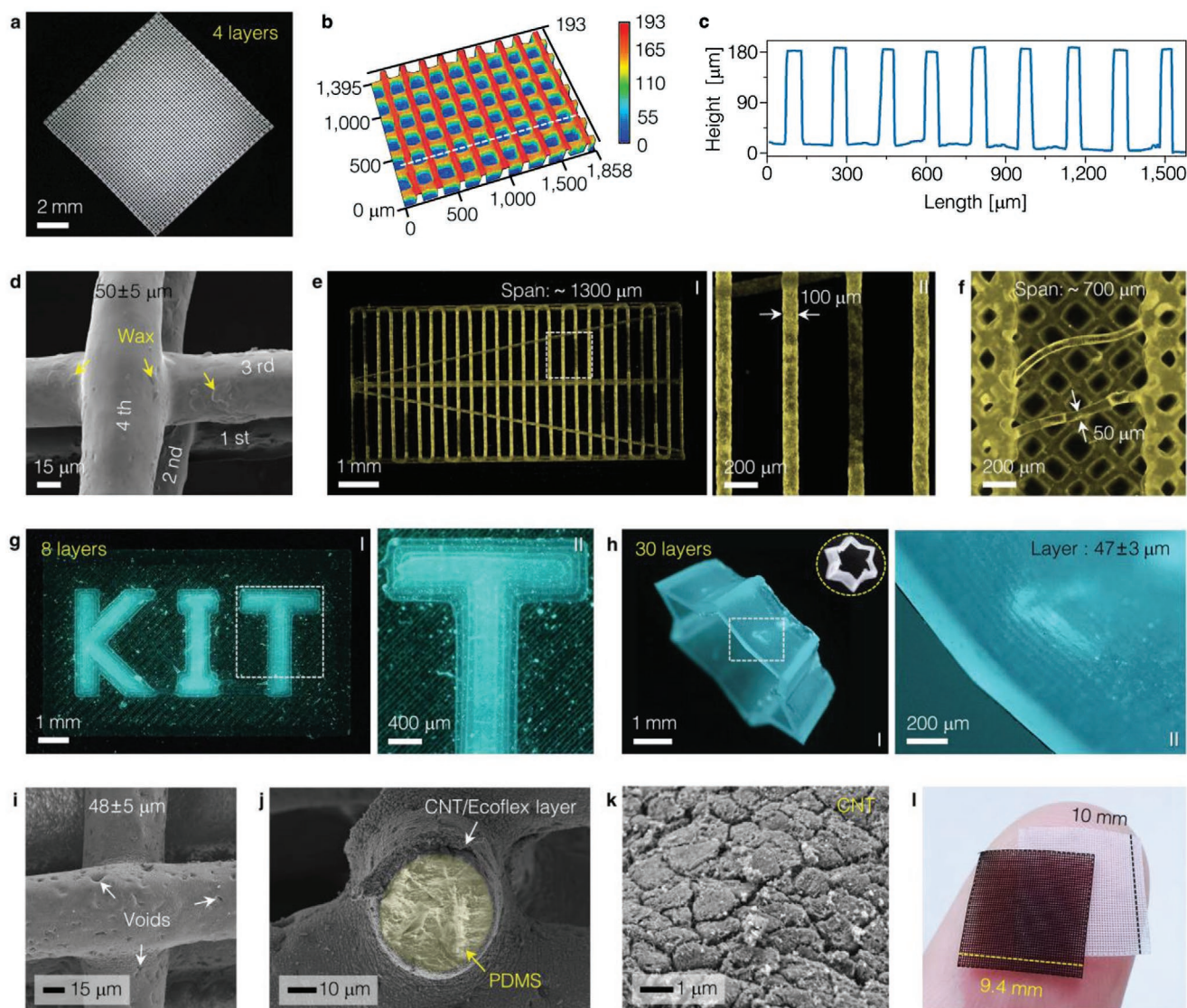


Figure 2. Morphology of printed soft objects. a) A 4-layer soft mesh (length and width, $10\ 150 \pm 50\ \mu\text{m}$; $T = 45\ ^\circ\text{C}$, $P = 70\ \text{bar}$, $V_p = 800\ \text{mm}\ \text{min}^{-1}$). b) The heightmap image of the mesh. c) The height information of the dashed line in the map (height, $193 \pm 10\ \mu\text{m}$). d) SEM image of the mesh. e,f) Span distance of the PSW ink during printing. The dark parts in the filaments indicate that the top filaments defect and contact the substrate. (f) is a magnified image of the marked part in Figure S3h (Supporting Information). g) An 8-layer soft KIT logo ($T = 45\ ^\circ\text{C}$, $P = 70\ \text{bar}$, $V_p = 750\ \text{mm}\ \text{min}^{-1}$). h) A 30-layer soft hollow star ($T = 45\ ^\circ\text{C}$, $P = 70\ \text{bar}$, $V_p = 750\ \text{mm}\ \text{min}^{-1}$). Every printed layer can be observed clearly in II (outer surface), and the thickness is $47 \pm 3\ \mu\text{m}$. i) SEM image of the mesh coated by CNT and Ecoflex. j) The cross-section of a filament in the conductive mesh. k) The magnified image of the CNT/Ecoflex layer. l) Two different meshes stacked on the finger. Note: apart from the object in (e), all silicone structures are printed by the $50\ \mu\text{m}$ nozzle with PSW ink. In (e), (g), and (h), (II) shows the magnified image of the marked section in (I).

electrodes in the mesh pore (Section III). The filament diameter (Figure S6d–f, Supporting Information) and mesh structure will influence the sensor performances, for example, the sensor with finer filaments has a higher sensitivity and lower critical pressure (Figure 3d,e). Increasing the layer number could increase the sensitivity of Sections II and III, and the critical pressure (Figure 3f and Figure S7a (Supporting Information)). On the contrary, decreasing the filament distance results in lower sensitivity, i.e., the slope of the $\Delta I/I_0$ versus pressure curve decreases (Figure 3f), which is attributed to the lack of spaces for contact and deformation. The deforming simulation of three different meshes under 24 kPa supplies more evidence

(Figure 3g). The $50D2L0.2d$ is pressed into a dense layer (Section III), while the $100D2L0.2d$ and $50D4L0.2d$ samples have more spaces for the deformation and are still in Section II. Besides, the mesh geometries have been supplied in the sensor names, for example, $50D2L0.2d$ means the sensing layer is printed by a $50\ \mu\text{m}$ nozzle ($50D$), and it has 2 layers ($2L$) with $0.2\ \text{mm}$ apart of filaments ($0.2d$). Due to the stable and hierarchical structure of the conductive mesh, the sensors show good repeatability for different pressures (Figure 3h), short response time ($72\ \text{ms}$) (Figure 3i), and excellent durability (Figure S7b, Supporting Information), which enable the tracking of blood pressure on the wrist (Figure 3j and Video S3 (Supporting Information))

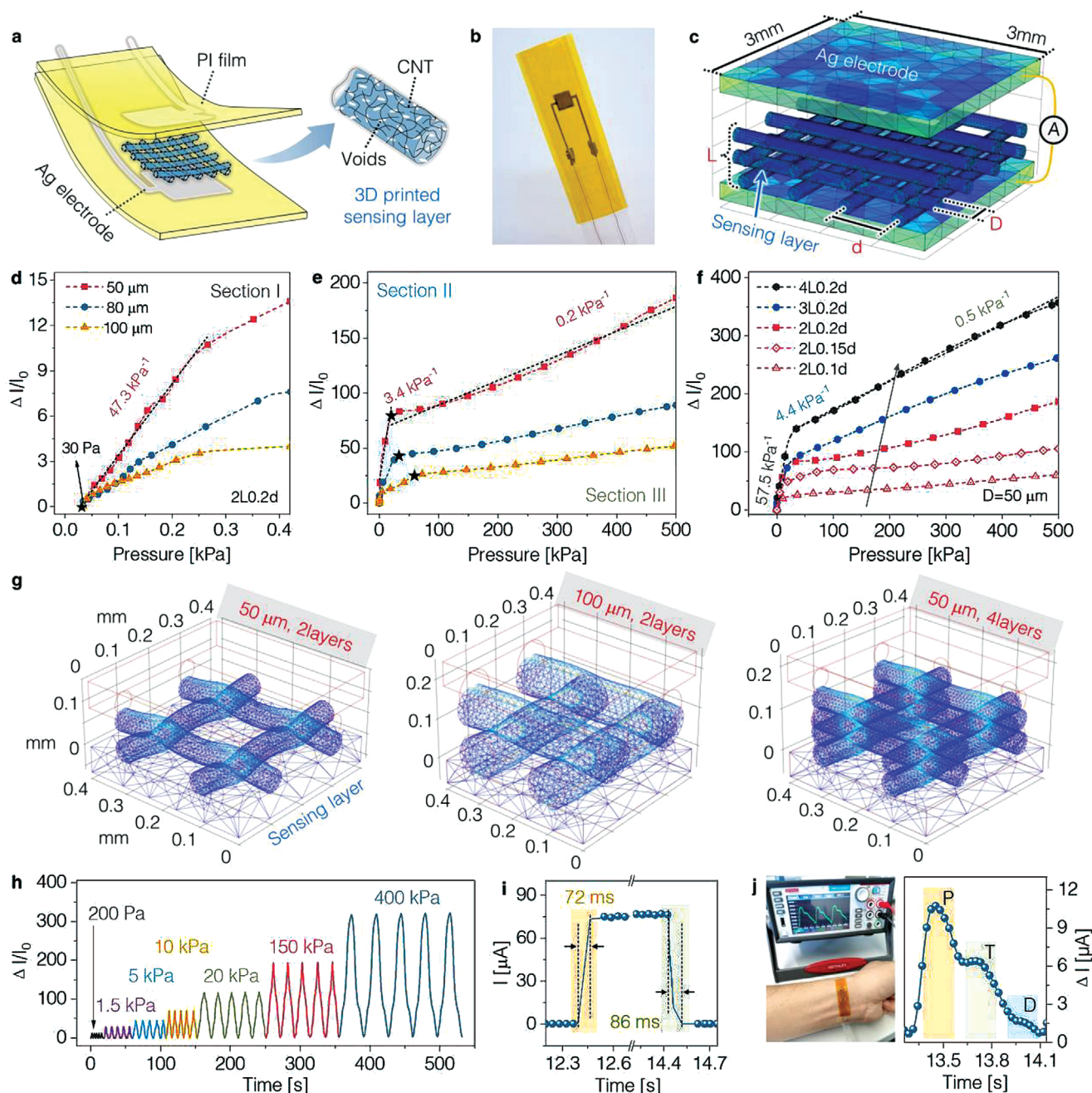


Figure 3. Flexible pressure sensors based on the 3D printed silicone meshes. a) Scheme for the device structure of flexible pressure sensor. b) A flexible pressure sensor. c) Schematic showing the sensing mechanism, which is influenced by layer number (L), the diameter of filament (D), and the distance between adjacent filaments (d). d,e) Relative current changes of different pressure sensors under pressure. The sensors (2L0.2d) have 2-layer meshes with 0.2 mm apart of filaments, which are printed by different nozzles (50, 80, and 100 μm). The critical pressures for the sensors have been marked by black stars, which are 24, 32, and 59 kPa, respectively. f) Influence of layer number and filament distance on relative current changes. The meshes are printed by a 50 μm nozzle. g) Deformation simulation of three meshes under the same pressure (24 kPa). The d is 0.2 mm. h) Relative current changes of 50D4L0.2d sensor (50D means the diameter is 50 μm) under different pressures. i) The response time and recovery time of 50D4L0.2d sensor. j) Arterial pulse signal monitored by the 50D4L0.2d sensor. The right photograph displays the detection process. The left part shows the waves with "P" (percussion), "T" (tidal), and "D" (diastolic) peaks.

and the detection of speaking (Figure S7c, Supporting Information). These high-performance pressure sensors can be used in the fabrication of soft robots, wearable and biomedical devices.^[1,6,7]

Soft silicone also shows the enormous capacity to fabricate smart soft devices inspired by nature.^[9,10,24] The new 3D

printing technology may enable to transform the bioinspired designs into practical devices and smart materials, such as superhydrophobic surfaces.^[24] According to reported work, the most critical part of superhydrophobic surface design is the synergistic action between dual-scale (micro- and nanoscale)

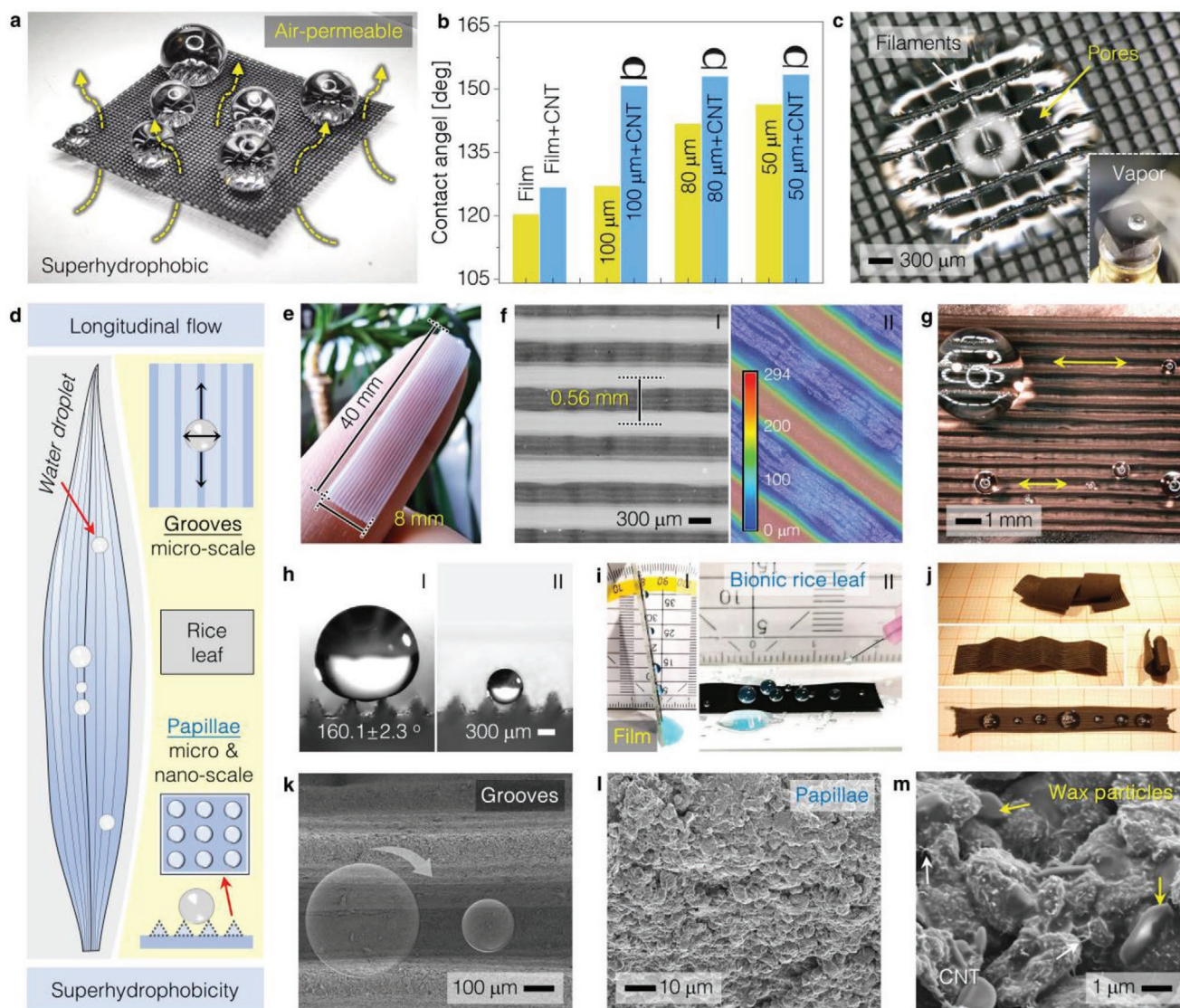


Figure 4. Bioinspired superhydrophobic devices based on 3D printed silicone objects. a) Photograph of the superhydrophobic bionic *Sarracenia* surface (50D4L0.2d), which supports 7 water droplets. b) Static contact angles of water on different silicone samples. 50, 80, and 100 μm represent the silicone meshes printed by PSW ink with the corresponding nozzles. CNT means the mesh has been coated with CNT and Ecoflex. c) The magnified image of the contact area between the water droplet and bionic *Sarracenia* surface. The inset image shows that the vapor is passing through the pores (Video S4, Supporting Information). d) Schematic illustration of the surface properties of rice leaf. e) 3D printed flexible groove structures inspired by rice leaf (80 μm nozzle, $T = 45^\circ\text{C}$, $P = 80$ bar, $V_p = 1500$ mm min^{-1}). f) Dark-field microscopy image (I) and heightmap image (II) of the printed groove structures. g) Photograph of the bionic rice leaf with water droplets on the surface. h) Side view images of the bionic rice leaf with big (I) and small (II) water droplets. i) Water transport on the PSW film (I) and the bionic rice leaf (II) (Video S4, Supporting Information). j) Shape-memory property of the bionic rice leaf. k–m) SEM images of the multiscale surface structures of the bionic rice leaf. Note: the wax still exists in the superhydrophobic mesh and bionic rice leaf.

structures and the intrinsic material hydrophobicity.^[35] The printed silicone mesh has been used to fabricate air-permeable, superhydrophobic surfaces with a fast water harvesting and transport capability (Figure 4a–c and Video S4 and Figure S8 (Supporting Information)) inspired by the *Sarracenia*. The CNT-coated silicone filaments have similar functions as the trichome, which are needle-shaped fibers ($\approx 1500\mu\text{m}$ in length, 30–55 μm in diameter) on the *Sarracenia* surface.^[36] They can capture dew and condense ambient moisture to form droplets, which will be transported on the surfaces quickly or drip. In addition, the

hydrophobic filaments could support the water droplets and the pores can keep good air permeability (Figure 4c). Although PDMS, wax, and CNT are hydrophobic, the contact angle of water on CNT-treated PSW film is only $126.6^\circ \pm 0.7^\circ$. With the same PSW ink, all the 3D printed bionic *Sarracenia* meshes are superhydrophobic, and finer filaments would create better superhydrophobicity, i.e., higher contact angle of water on that substrate (Figure 4b). Besides, due to the stretchable substrate and CNT/Ecoflex layer, the devices have good durability (Figure S9, Supporting Information).

Inspired by the rice leaf (Figure 4d), we printed a soft silicone film with many grooves (Figure 4e and Figure S8e (Supporting Information)). Small droplets merge in the grooves formed by the triangular-shaped veins, resulting in a longitudinal flow on the rice leaf.^[37] Such microscale structures have been duplicated in our bionic rice leaf with the HOT-DIW printing strategy (Figure 4f). The superhydrophobicity of the rice leaf is attributed to the tapered micropapillae and the superficial waxy nanobumps.^[38] To obtain a similar performance, we deposited CNT on the bionic rice leaf without removing the wax, thus creating a dual-scale structure.^[10] The bionic rice leaf shows a good superhydrophobicity with a contact angle of $160.1^\circ \pm 2.3^\circ$ (Figure 4g,h). The array of sinusoidal grooves enables the longitudinal flow of small water droplets (Figure 4g). Figure 4i compares the water transport capacity of PSW film and the bionic rice leaf (Video S5, Supporting Information), the flat film (I) has to be tilted ($\approx 80^\circ$) to enable the gravity-driven flow. By contrast, on the grooved rice leaf (II) flow takes place even almost horizontally (tilt angle $< 5^\circ$), which is further evidence of the advantages of the new strategy in bionics.

Furthermore, the wax in the soft bionic rice leaf could endow it with a good shape-memory property (Figure 4j and Video S6 (Supporting Information)). The soft leaf can be transformed into different shapes at a high temperature without degrading the superhydrophobicity. Another heating treatment will recover the original shape of the bionic leaf. SEM images (Figure 4k–m) supply more information about geometric characteristics, which includes the microscale grooves and papillae, and the nanoscale structures formed by CNT, wax, and Ecoflex.

3. Conclusion

We present a simple and powerful 3D printing strategy for manufacturing soft silicone objects with high resolution and good shape fidelity. By constructing temperature-sensitive particle networks in the ink and adjusting the nozzle temperature, we can control the rheological properties of viscoelastic ink rapidly and avoid the gravity-induced deformation of the printed structures. A broad range of minimized, bionic, and biocompatible silicone architectures can be patterned by the new 3D printing method, illustrating its capability in the personalized manufacturing of soft materials. The high resolution and rich microstructures of printed silicone extend its applications in flexible electronics, driving the flexible electronics close to the practical applications and market. In addition, the ease of functionalization and the multimaterial printing of HOT-DIW technology enables the fabrication of soft bioinspired devices with spatially varying functions, such as air permeability, superhydrophobic, and shape memory. We believe that this technology will accelerate the fabrication of soft materials with multiscale structures and the desired functions, thereby leading to more capable smart devices, soft robots, and flexible electronics.

4. Experimental Section

PDMS-Based Ink Preparation: First, 6 g PDMS part A (Sylgard 184, Dow Corning), 1.2 g silica nanoparticle (fumed silica, <70 nm, $130\text{--}170$ m² g⁻¹, Alfa Aesar), and an amount of paraffin wax (Sasolwax 5405, Sasol

Performance Chemicals) were mixed with 3 g cyclohexane (Acros Organics) in the planetary mixer (SpeedMixer, Hauschild & Co. KG, Germany) at 3500 rpm for 10 min total (5 times). Then, the mixtures were stored in a fume cupboard for 48 h to remove the cyclohexane. Finally, 0.6 g PDMS part B was added to the mixture in the planetary mixer at 2000 rpm for 2 min. The PS ink was prepared in the same manner. The formulations of PDMS-based inks were listed in Table S1 (Supporting Information). All the inks were stored at a low temperature (-20°C) before printing.

Fabrication of the Nozzle Temperature Control System: A commercial carbon black/poly(ethylene terephthalate) (PET) electric heater band was used as the flexible heater. A self-made CNT/silicone elastomer (Ecoflex 00-30; Smooth-On Inc.) composite was used to fill the space between the zirconia alumina nozzle (Small Precision Tools Roth AG, Switzerland) and the heater. A commercial temperature control unit (XY-T01, Drok) was used to supply current to the heater based on real-time temperature data supplied by a thermometer directly mounted to the heater (Figure S1a, Supporting Information). Besides, the temperature control system was calibrated using a high-precision commercial thermometer (TH1, Domotherm).

Printing of Soft Silicone Objects: The 3D printing of PSW ink was conducted on a high-precision 3D printer (Voxel8 Developer's Kit printer) in pneumatic mode. Three kinds of high-precision zirconia alumina nozzles with different internal diameters (100, 80, and 50 μm) were chosen for printing (Figure S1b, Supporting Information). During printing, the extrusion pressure (P) and printhead speed (V_p) were set by the software, while the nozzle temperature (T) was controlled by the temperature control system. Various configurations of 3D structures were designed with commercial software (3ds Max) and converted to the corresponding G-codes by another commercial software (Cura, Ultimaker). These G-codes were modified with the commercial software (Repetier, Hot-World GmbH & Co. KG) further. The soft silicone objects were printed on a PET film and left to cross-link at room temperature for 1 week. Then, they were transferred to an oven (100°C) for another 24 h.

Preparation of the Sensing Layers for Flexible Pressure Sensors: First, a certain amount of CNT (TNIM4, Chengdu Organic Chemicals Co., Ltd.) and the 3D printed silicone meshes were put in the plastic box for high shear stirring in the planetary mixer at 3500 rpm for 5 min. This procedure generated heat sufficient to melt the wax particles partly, thus enabling the CNT adhesion to the silicone surface. Second, after cooling to room temperature, the obtained samples were put into mineral spirits (Sigma-Aldrich, Inc.) for 1 min while slowly stirring. Mineral spirits swelled the silicone and dissolved the wax particle, thus creating rough surfaces supporting the adhesion of the CNT. Third, the meshes were transferred into pure ethanol for removing the mineral spirits and wax, that shrunk the silicone meshes and created many voids strengthening the adhesion of CNT. The second and third steps or the swelling–shrinking process were repeated 3 times (Video S2, Supporting Information). After removing all the solvents, the treated meshes were dipped in 10 wt% Ecoflex-30 mineral spirits solution for 10 s and then transferred onto absorbing paper for removing the excess solution. At last, the conductive meshes were obtained through a high-temperature treatment in an oven (100°C) for 12 h cross-linking the Ecoflex-30. The preparation process of the sensing layer from the printed silicone meshes is illustrated in Figure S5 (Supporting Information).

Fabrication of the Flexible Pressure Sensors: First, a designed paper mask was prepared using a commercial CO₂ laser cutting machine (DAJA-D02, Diaojiang Co., Ltd.). Then, the paper mask was put on the targeted PI films (Kapton EN 25 μm , DuPont), followed by screen printing of the silver ink (05002-AB, Structure Probe, Inc.). After removing the mask, the Ag/PI electrode film was heated at 80°C for 10 min. Two copper wires were connected to the electrode layer at two ends with silver paint and tempered at 80°C for 30 min. The sensing layer was assembled in the middle of two Ag/PI electrodes. After gluing the PI films with the biaxially oriented polypropylene tape, the flexible pressure sensors were fabricated successfully.

Preparation of the Bionic Sarracenia Surfaces and Bionic Rice Leaf: The bionic *Sarracenia* surfaces were printed in the same manner as

the silicone meshes. For the bionic rice leaf, the PSW ink was used to print the flexible groove structure with the 80 μm nozzle. The printing temperature, extrude pressure, and nozzle speed were 45 $^{\circ}\text{C}$, 80 bar, and 1500 mm min^{-1} , respectively. The cross-linking process was kept the same as for the other printed objects. It was noted that only the high shear stirring and coating processes were needed for the coating of the CNT/Ecoflex layer. The wax still existed in the bionic *Sarracenia* surfaces and bionic rice leaf, which helped to bring about excellent superhydrophobicity and shape-memory properties.

Device Characterization: The electrical signals of the pressure sensors were measured using a digital source meter (Keithley 2450) at a constant voltage of 0.1 V. The pressure loading was performed using a universal testing machine (TA-XT Plus Texture Analyzer). Before the tests, 500 training cycles were needed for each sensor to achieve a stable operational state. For the sensitivity tests and the response time tests, the loading rates were 0.1 and 10 mm s^{-1} , respectively. For the detections of the arterial pulse and sound signals, the sensors were attached to the wrist and throat, respectively. For cyclic loading–unloading of pressure, the sensor was placed on the testing system and a preselected constant pressure was repeatedly applied and released while the transient electrical signal was recorded. The deformation simulation of the sensing layers under 24 kPa was performed using the COMSOL Multiphysics software package (COMSOL Inc., USA).

Rheological Measurements: The rheological properties of the PDMS-based ink were measured using a rotational rheometer (MCR501, Anton Paar GmbH) equipped with a parallel plate (25 mm) fixture, a gap distance of 1 mm was selected. To measure the storage modulus G' and loss modulus G'' at different temperatures (20, 45, and 60 $^{\circ}\text{C}$), frequency sweep tests (100–0.01 rad s^{-1}) were conducted in the linear viscoelastic region at a strain of 0.05%. For the yield stress τ_y , stress ramps were applied covering the shear stress range of 10–50 000 Pa. The yield stress was determined from the deformation versus shear stress curves according to the tangent intersection method.^[27] To characterize the collapse and recovery of the wax network, the three interval thixotropy test was conducted using the following signal sequence: 120 s at a shear strain of 0.05% (small amplitude oscillatory shear), 120 s at a shear strain of 5% (large amplitude oscillatory shear), 360 s at a shear strain of 0.05% (recovery), in all steps a constant frequency of 10 rad s^{-1} was employed.

Morphological Analysis and Other Characterizations: The morphologies of the 3D printed objects and the CNT particles were characterized using SEM (S-4500, Hitachi High-Technologies Europe GmbH) and optical microscopy (VHX, Keyence). The optical microscope was also used to measure the diameters of the PSW filaments extruded with different nozzles at several temperatures. The phase change of wax was characterized by differential scanning calorimetry (Universal V4.5A TA Instruments) analysis in a range from -20 to 90 $^{\circ}\text{C}$ with 10 $^{\circ}\text{C min}^{-1}$ heating and cooling rates. Contact angles of deionized water on 3D printed objects were measured using the sessile drop method (SCA 20, DataPhysics Instruments GmbH), evaluated by a numerical Young–Laplace fit. To display the water harvesting of the bionic *Sarracenia* surface, a commercial ultrasonic humidifier (SCK-3Q40, Midea Group) was used to generate vapor. The shape-memory property of the bionic rice leaf was characterized by an optical microscope combined with a hot air gun (RT-HA 2000E, ISC GmbH), which enabled the observation of the shape and recovery.

Supporting Information

Supporting Information is available from the Wiley Online Library or from the author.

Acknowledgements

The authors acknowledge the financial support by Helmholtz Association and The Office of China Postdoctoral Council.

Open access funding enabled and organized by Projekt DEAL.

Conflict of Interest

The authors declare no conflict of interest.

Data Availability Statement

The data that support the findings of this study are available from the corresponding author upon reasonable request.

Keywords

3D printing, bionic surfaces, flexible electronics, phase-change ink, soft silicone

Received: November 15, 2021

Revised: January 30, 2022

Published online:

- [1] S. I. Rich, R. J. Wood, C. Majidi, *Nat. Electron.* **2018**, *1*, 102.
- [2] Y. Kim, H. Yuk, R. Zhao, S. A. Chester, X. Zhao, *Nature* **2018**, *558*, 274.
- [3] M. Wehner, R. L. Truby, D. J. Fitzgerald, B. Mosadegh, G. M. Whitesides, J. A. Lewis, R. J. Wood, *Nature* **2016**, *536*, 451.
- [4] W. Hu, G. Z. Lum, M. Mastrangeli, M. Sitti, *Nature* **2018**, *554*, 81.
- [5] L.-y. Zhou, J.-z. Fu, Q. Gao, P. Zhao, Y. He, *Adv. Funct. Mater.* **2019**, *30*, 1906683.
- [6] Y. Gao, L. Yu, J. C. Yeo, C. T. Lim, *Adv. Mater.* **2020**, *32*, 1902133.
- [7] M. Cianchetti, C. Laschi, A. Menciassi, P. Dario, *Nat. Rev. Mater.* **2018**, *3*, 143.
- [8] I. R. Mineev, P. Musienko, A. Hirsch, Q. Barraud, N. Wenger, E. M. Moraud, J. Gandar, M. Capogrosso, T. Milekovic, L. Asboth, R. F. Torres, N. Vachicouras, Q. Liu, N. Pavlova, S. Duis, A. Larmagnac, J. Vörös, S. Micera, Z. Suo, G. Courtine, S. P. Lacour, *Science* **2015**, *347*, 159.
- [9] M. Schaffner, J. A. Faber, L. Pianegonda, P. A. Ruhs, F. Coulter, A. R. Studart, *Nat. Commun.* **2018**, *9*, 878.
- [10] D. Wang, Q. Sun, M. J. Hokkanen, C. Zhang, F. Y. Lin, Q. Liu, S. P. Zhu, T. Zhou, Q. Chang, B. He, Q. Zhou, L. Chen, Z. Wang, R. H. A. Ras, X. Deng, *Nature* **2020**, *582*, 55.
- [11] H. Yuk, X. Zhao, *Adv. Mater.* **2018**, *30*, 1704028.
- [12] Z. C. Eckel, C. Zhou, J. H. Martin, A. J. Jacobsen, W. B. Carter, T. A. Schaedler, *Science* **2016**, *351*, 58.
- [13] M. A. Skylar-Scott, J. Mueller, C. W. Visser, J. A. Lewis, *Nature* **2019**, *575*, 330.
- [14] S. Gantenbein, K. Masania, W. Woigk, J. P. W. Sesse, T. A. Tervoort, A. R. Studart, *Nature* **2018**, *561*, 226.
- [15] S. Roh, D. P. Parekh, B. Bharti, S. D. Stoyanov, O. D. Velev, *Adv. Mater.* **2017**, *29*, 1701554.
- [16] R. L. Truby, J. A. Lewis, *Nature* **2016**, *540*, 371.
- [17] L. Y. Zhou, J. Fu, Y. He, *Adv. Funct. Mater.* **2020**, *30*, 2000187.
- [18] L. Y. Zhou, Q. Gao, J. Z. Fu, Q. Y. Chen, J. P. Zhu, Y. Sun, Y. He, *ACS Appl. Mater. Interfaces* **2019**, *11*, 23573.
- [19] E. Koos, N. Willenbacher, *Science* **2011**, *331*, 897.
- [20] C. Perrinet, E. J. Courtial, A. Colly, C. Marquette, R. Fulchiron, *Adv. Mater. Technol.* **2020**, *5*, 1901080.
- [21] R. Karyappa, T. Ching, M. Hashimoto, *ACS Appl. Mater. Interfaces* **2020**, *12*, 23565.
- [22] C. S. O'Bryan, T. Bhattacharjee, S. Hart, C. P. Kabb, K. D. Schulze, I. Chilakala, B. S. Sumerlin, W. G. Sawyer, T. E. Angelini, *Sci. Adv.* **2017**, *3*, 1602800.
- [23] S. R. A. Ruth, V. R. Feig, H. Tran, Z. Bao, *Adv. Funct. Mater.* **2020**, *30*, 2003491.

- [24] S. Li, H. Bai, R. F. Shepherd, H. Zhao, *Angew. Chem., Int. Ed.* **2019**, *58*, 11182.
- [25] T. J. Wallin, J. Pikul, R. F. Shepherd, *Nat. Rev. Mater.* **2018**, *3*, 84.
- [26] J. W. Boley, K. Chaudhary, T. J. Ober, M. Khorasaninejad, W. T. Chen, E. Hanson, A. Kulkarni, J. Oh, J. Kim, L. K. Aagesen, A. Y. Zhu, F. Capasso, K. Thornton, P. V. Braun, J. A. Lewis, *Adv. Mater.* **2017**, *29*, 1604778.
- [27] C. Yuce, N. Willenbacher, *J. Visualized Exp.* **2017**, *122*, e55377.
- [28] J. E. Smay, J. Cesarano, J. A. Lewis, *Langmuir* **2002**, *18*, 5429.
- [29] D. C. Kim, H. J. Shim, W. Lee, J. H. Koo, D. H. Kim, *Adv. Mater.* **2019**, *32*, 1902743.
- [30] C. Ma, D. Xu, Y. C. Huang, P. Wang, J. Huang, J. Zhou, W. Liu, S. T. Li, Y. Huang, X. Duan, *ACS Nano* **2020**, *14*, 12866.
- [31] L. Qian, Y. Xie, S. Zhang, J. Zhang, *Matter* **2020**, *3*, 664.
- [32] S. Wang, J. Xu, W. Wang, G. N. Wang, R. Rastak, F. Molina-Lopez, J. W. Chung, S. Niu, V. R. Feig, J. Lopez, T. Lei, S. K. Kwon, Y. Kim, A. M. Foudeh, A. Ehrlich, A. Gasperini, Y. Yun, B. Murmann, J. B. Tok, Z. Bao, *Nature* **2018**, *555*, 83.
- [33] C. Zhang, H. Li, A. Huang, Q. Zhang, K. Rui, H. Lin, G. Sun, J. Zhu, H. Peng, W. Huang, *Small* **2019**, *15*, 1805493.
- [34] Y. Wang, H. Wang, H. Wang, M. Zhang, X. Liang, K. Xia, Y. Zhang, *ACS Appl. Mater. Interfaces* **2019**, *11*, 20272.
- [35] Y. Si, Z. Dong, L. Jiang, *ACS Cent. Sci.* **2018**, *4*, 1102.
- [36] H. Chen, T. Ran, Y. Gan, J. Zhou, Y. Zhang, L. Zhang, D. Zhang, L. Jiang, *Nat. Mater.* **2018**, *17*, 935.
- [37] M. Song, D. Hu, X. Zheng, L. Wang, Z. Yu, W. An, R. Na, C. Li, N. Li, Z. Lu, Z. Dong, Y. Wang, L. Jiang, *ACS Nano* **2019**, *13*, 7966.
- [38] G. D. Bixler, B. Bhushan, *Soft Matter* **2012**, *8*, 11271.